Highlights

Influence of turbulent natural convection on heat transfer in shallow caves

B. Qaddah, L. Soucasse, F. Doumenc, S. Mergui, Ph. Rivière, A. Soufiani

- Large-eddy simulations of natural convection in a confined shallow cave are performed using wall temperature distributions representative of different times of the year.
- We propose a general approach to predict heat transfer in a shallow confined cave, and analyse the role of convection and radiation.
- Two flow regimes are found depending on the direction of the mean vertical temperature gradient.
- Heat transfer coefficients are calculated from the simulations and the use of the Newton's law to predict the heat flux at cave walls is discussed.

Influence of turbulent natural convection on heat transfer in shallow caves

B. Qaddah[a], L. Soucasse[a], F. Doumenc[b,c], S. Mergui[b,c], Ph. Rivière[a], A. Soufiani[a]

[a] *Laboratoire EM2C, CNRS, CentraleSupélec, Université Paris-Saclay, 8-10 rue Joliot Curie, 91192 Gif-sur-Yvette, France*
[b] *Université Paris-Saclay, CNRS, FAST, 91405, Orsay, France*
[c] *Sorbonne Université, UFR 919, 4 place Jussieu, F-75252, Paris Cedex 05, France*

Abstract

We aim at analyzing in detail the different heat transfer mechanisms involved in a confined shallow cave embedded in a rock massif submitted to seasonal variations of the ground temperature. Heat conduction in the rock massif, radiative heat transfer between cave walls, and turbulent natural convection inside the cave are considered. The natural convection problem is solved by large-eddy simulations (LES) using a Chebyshev pseudo-spectral method associated with a spectral vanishing viscosity (SVV) model. The thermal boundary conditions applied to the cave walls are obtained from a large-scale model that takes into account heat conduction in the rock massif and radiative fluxes between cave walls. This approach allows us to characterize the relative strength of convective and radiative fluxes and to identify the regions of the cavity and times of the year of intense heat transfer. We identified two different flow regimes: (i) a one-cell flow regime associated with strong convection, high turbulence level and unstable mean vertical temperature gradient, (ii) a multiple-cell flow regime associated with weak convection, low turbulence level and stable mean vertical temperature gradient. The use of the Newton's law to describe convection heat fluxes at the cavity walls is discussed.

Keywords: Shallow caves, Turbulent natural convection, Heat transfer, Large-eddy simulation, Spectral vanishing viscosity

---

Email address: qaddah.baraa@centralesupelec.fr (B. Qaddah)

1. Introduction

Karsts are landscapes formed from the dissolution of soluble rocks, for instance limestone or gypsum [1]. The chemical erosion due to rainwater results in the formation of an extensive network of caves. Heat transfer in karstic massifs is at the core of many issues, as diverse as paleoclimate reconstruction from speleothem analysis [2], consequences of tunneling on the environment [3], evolution of subterranean flora and fauna [4], or conservation of parietal prehistoric paintings [5, 6]. However, assessing temperature fields and heat fluxes in karstic massifs is complicated by the coupling between several heat transfer mechanisms, as heat conduction in the rock and convection due to air and water circulation in caves [7], possibly with latent heat exchanges due to condensation/evaporation or even ice formation [8].

In this work, we focus on caves located at a shallow depth, typically on the order of 10 meters. This configuration corresponds to that of many painted caves in France (Lascaux [9], Marsoulas and Pech Merle [10]) and throughout the world (Altamira in Spain [5], Takamatsuzuka Tumulus in Japan [11]). The exceptional state of conservation of parietal paintings (some of which are more than 10,000 years old) is mainly due to the high stability of cave microclimate. Painting damages can occur when this microclimate is disturbed. Human visits may result in significant climate perturbations in a number of different ways, directly (increase in temperature, humidity and CO_2 concentration, resulting in enhanced condensation and corrosion on cave walls [12]) or indirectly (need for an artificial ventilation, modification of cave entrance to allow visits as in Lascaux [9] or Marsoulas [10]). In some cases, the cessation or the limitation of visits is not enough to restore favourable conditions for conservation, and remediation may be necessary (e.g., thermal insulation of the Takamatsuzuka Tumulus [11]). A deep understanding of the physical mechanisms driving heat transfer inside a cave and between a cave and its external environment is therefore necessary to improve the conservation of painting cave heritage.

The damping of the external temperature fluctuations by the rock massif surrounding a confined cave is the main reason for its high thermal stability (by confined cave, we mean a cave for which mass transfer with the external environment can be neglected). Quindos and coworkers [13, 5] measured the amplitude and phase shift of the annual temperature variations at the roofs of Altamira Cave, at different locations of varying depth (from 3.5 m to 17.5 m), and found a good agreement with the prediction of the periodic

1D conduction model. In the range of depth from a few meters to approximately 10 m, daily temperature fluctuations can be considered as completely damped, while annual temperature fluctuations are still perceptible.

Due to complex cave geometry and depth variations all along the cave, temperature levels inside the cave (i.e., wall and air temperatures) vary not only in time, but also in space. Quindos *et al* [5] found that the amplitude and phase shift at the floors of Altamira Cave were close to the values measured at the roofs, which they attributed to radiative heat transfer between cave walls. Guerrier *et al* [14] confirmed by numerical simulations the significant role of thermal radiation in the homogenization of the temperature field inside a confined cave. However, spatial temperature variations are not strictly zero. For instance, temperature differences on the order of 0.1 K were commonly measured between the walls of the Hall of Bulls in Lascaux Cave [15]. This is enough to trigger significant natural convection flow. Indeed, assuming a cave height of 5 m, the Rayleigh number comparing buoyancy and diffusion is on the order of 10^9, denoting possible turbulent flow at least in some parts of the cave [16, 17]. In addition, relative humidity is often close to 100 % in confined caves [5, 10], due to the presence of thin liquid films of percolating water on the walls and weak ventilation. Therefore, small temperature variations can induce condensation/evaporation at the walls, so that latent heat exchange must be considered. Due to seasonal variations of water intake [18], air humidity [5] and wall temperatures, condensation/evaporation mass fluxes are expected to vary in time. In conclusion, a minimal model for a shallow confined cave must consider heat conduction in the rock massif, radiative heat transfer between cave walls, and turbulent natural convection inside the cave. In addition, the significance of latent heat exchanges due to condensation and evaporation must be assessed.

The numerical investigation of cave climate is clearly restricted by the computational effort required to simulate 3D turbulent natural convection. If the gas is assumed to be transparent, radiative transfer between opaque walls can be efficiently computed using view factors. A simple approach to account for convection without solving the Navier–Stokes equations is to estimate the wall convective heat fluxes from the Newton's law [11, 14]. A considerable drawback of this method is the need for empirical correlations to estimate heat transfer coefficients, whereas available correlations refer to cavities of simple geometry with uniform thermal boundary conditions on each wall [19]. These conditions are far from being fulfilled in natural cavities, making the estimation of heat transfer coefficients inaccurate. In contrast, some authors rely on Computational Fluid Dynamics (CFD) to get better insights on convection in caves [6, 20]. Assuming laminar flow, Lacanette *et al.* [20] developed specific numerical methods to solve for air velocity, temperature and moisture fields in Lascaux cave. Two sets of prescribed boundary conditions, representative of climate conditions in 1980 and 1999, were considered.

In this article, we aim at analyzing in detail the different mechanisms involved in heat transfer in a confined shallow cave embedded in a rock massif. Ideally, we should consider a problem where heat conduction in the rock, radiative transfer between the cave walls, and turbulent natural convection inside the cave are fully coupled, and solve a 1–year periodic regime. However, a one–year CFD simulation is not practicable with current computational resources. We thus proceed as follows. We first define a large–scale model, including heat conduction in the rock massif and radiative heat transfer between the cave walls, but neglecting convection inside the cave. Solving the periodic regime provides temperature fields in the rock massif (including the cave walls) all along the year. Then we select six wall temperature fields (spaced two months apart) representative of the different thermal states encountered in the cave over the year. These temperature fields are used as boundary conditions to solve the natural convection problem inside the cave by a detailed flow simulation.

The thermal conductive fluxes in the air at the cave walls (i.e., the thermal "convective" fluxes) obtained from the detailed flow simulation are then compared with the radiative fluxes predicted by the large–scale model. Two cases may arise:

- the thermal conductive fluxes at the cave walls are much smaller than the radiative fluxes, and disregarding convection in the large–scale model was a valid assumption. The temperature and velocity fields inside the cave are known from the detailed flow simulation. If humid air was considered, the vapor concentration field in the cave and evaporation/condensation mass fluxes at the cave walls would also be known.

- the thermal conductive fluxes at the cave walls are larger than the radiative fluxes. In this case, natural convection significantly contributes to the uniformization of the wall temperature fields. Since this effect was not taken into account in the large–scale model, the intensity of the natural convection flow is likely overestimated. Conduction fluxes at the cave walls can thus be regarded as higher bounds of the actual ones, which is still a useful information. This approach also provides higher bounds of evaporation/condensation mass fluxes when humid air is considered.

For the sake of simplicity, we consider a parallelepiped cavity, but more complex geometries could be treated with the same global approach. As a first step, we only consider in this article the limiting case of dry air (latent heat exchanges are thus disregarded). The large–scale model is solved using the finite element method. The turbulent convection flow inside the cave is obtained from large-eddy simulations (LES) performed with a Chebyshev pseudo-spectral method associated with a spectral vanishing viscosity (SVV) model [21].

The paper is organised as follows. We first describe the large-scale model used to obtain temperature fields at cave walls (Sec. 2). Then we present the LES model used for the simulation of the natural convection flow inside the cave, and its numerical validation (Sec. 3). We discuss in section 4 the different flow regimes observed depending on the season, as well as turbulent statistics. We analyse in section 5 the heat flux distributions at the walls. Conducto-convective fluxes are compared with radiative fluxes. Concluding remarks are presented in section 6.

2. Large–scale model

2.1. Governing equations

The large–scale model is a 3D extension of the 2D model defined by Guerrier *et al* [14]. We consider the confined parallelepiped cavity embedded in the rock massif displayed in Fig. 1a. The ground surface is inclined at 10° from the horizontal direction. The left upper edge of the cavity is located at a depth of 7.3 m. The cave dimensions are the height $L_X = 5.3\,\mathrm{m}$, the width $L_Y = 7\,\mathrm{m}$ and the length $L_Z = 17\,\mathrm{m}$ (see Fig. 2a), which roughly reflect the size of the Hall of Bulls in Lascaux Cave. The gravity acceleration field corresponds to $\boldsymbol{g} = -g\boldsymbol{X}$.

Conductive heat transfer is assumed in the rock massif:

$$\frac{\partial T_r}{\partial t} = \alpha_r \boldsymbol{\nabla}^2 T_r \,, \tag{1}$$

where T_r is the rock temperature, t the time and $\alpha_r = 8 \times 10^{-7}\,\mathrm{m}^2.\mathrm{s}^{-1}$ the limestone diffusivity [14]. A time–periodic Dirichlet condition is imposed at

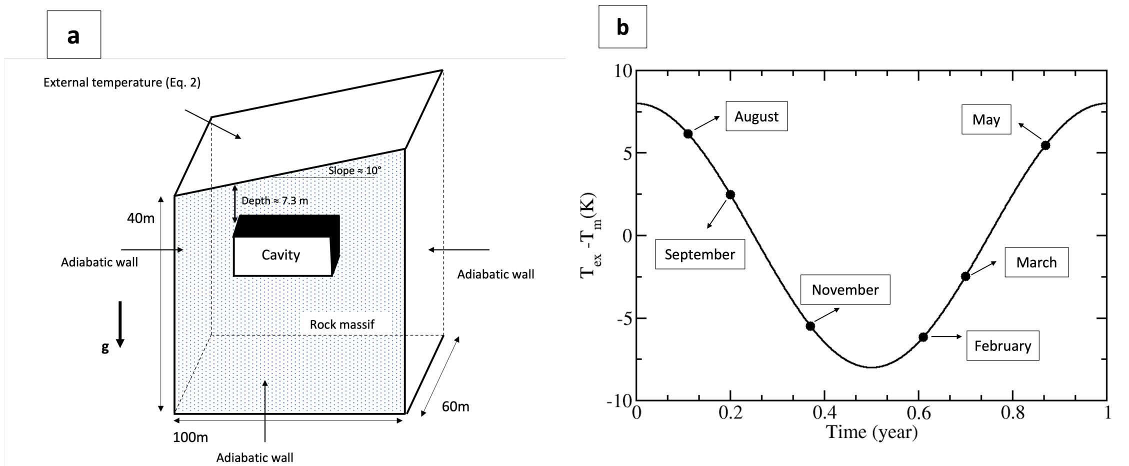

Figure 1: a) Geometry setup for the large–scale model (not at scale). b) Time evolution over a one-year period of the external temperature fluctuation $T_{ex}(t) - T_m$ applied at the upper surface of the massif. The six filled circles correspond to the six months that we investigate (see the corresponding times in Tab. 1).

the upper surface of the rock massif (see Fig. 1a):

$$T_{ex}(t) = T_m + A\cos\left(2\pi\frac{t}{\tau}\right) , \tag{2}$$

where T_{ex} is the external ambient temperature, $\tau = 1\,\text{year}$ is the period, $T_m = 12°\text{C}$ is the annual average external temperature and $A = 8°\text{C}$ is the amplitude of the temperature variations (these values of T_m and A are typical of the climate conditions in south–west of France). The time evolution of T_{ex} is displayed in Fig. 1b, where the six months that will be investigated using the LES model are highlighted. As we only consider the periodic regime, we arbitrarily assume that the initial time corresponds to the hottest temperature of the year that takes place in July.

The lateral and bottom sides of the massif are adiabatic. With the approximation of black walls (the emissivity of limestone is 0.96 [19], i.e., close to 1), and disregarding convection as explained in the introduction, the boundary condition at cave walls reads

$$-\lambda_r \boldsymbol{\nabla} T_r.\boldsymbol{n} = \sigma T^4 - \int_{\boldsymbol{\Omega}\cdot\boldsymbol{n}<0} I(\boldsymbol{\Omega})|\boldsymbol{\Omega}\cdot\boldsymbol{n}|d\boldsymbol{\Omega}\,, \tag{3}$$

where $\lambda_r = 1.656\,\text{W.m}^{-1}.\text{K}^{-1}$ is the rock thermal conductivity [14], $\boldsymbol{n}$ is the normal vector pointing to the cavity, σ is the Stefan-Boltzmann constant

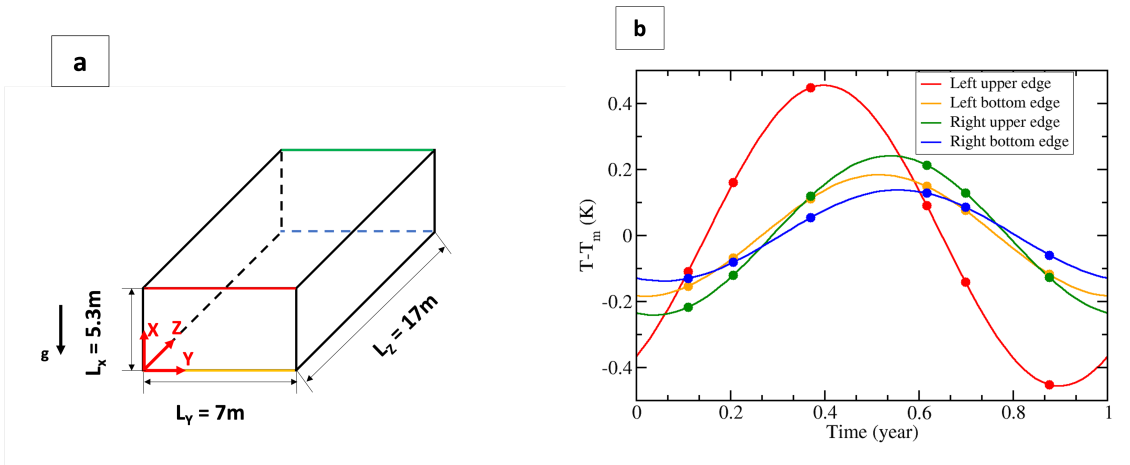

Figure 2: a) Geometry setup of the cavity. b) Time evolution of the temperature fluctuations $T(t) - T_m$ averaged on four edges of the cave. Red, yellow, green and blue lines correspond to the left upper ($Z = 0$ and $X = L_X$), left bottom ($Z = 0$ and $X = 0$), right upper ($Z = L_Z$ and $X = L_X$) and right bottom ($Z = L_Z$ and $X = 0$) edges, respectively (the colors of the edges in Fig. 2a, and of the curves in Fig. 2b correspond to each other). The six months that we investigate are marked with filled circles.

and $I(\mathbf{\Omega})$ is the radiative intensity (integrated over the infrared spectrum) in direction $\mathbf{\Omega}$. The air is supposed to be transparent. Therefore, $I(\mathbf{\Omega})$ depends on wall temperatures, and does not depend on the temperature field of the gas phase.

The model defined by Eqs.(1-3) is solved using the commercial software Comsol Multiphysics (Galerkin method, time discretization based on implicit backward differentiation formulas). The computational domain is discretized with a total of approximately 530,000 quadratic Lagrangian tetrahedron elements. The view factors related to surface elements on cave walls are calculated using the hemicube method [22].

2.2. Results from the large–scale model

We discuss the six wall temperature fields resulting from the simulation of the large–scale model, at months of the year indicated in Fig. 1b. The wall temperature fields in February, March and May are displayed in Fig. 3. The wall temperature fields for the months of August, September and November (not shown) can be deduced by symmetry from those of February, March and May respectively, thanks to the yearly periodicity. Despite the simple geometry of the cave, the wall temperature fields are rather complex. Because of conductive damping in the rock and temperature uniformization by radiative transfer inside the cavity, temperature gradients are larger along the vault than along the floor, the latter being quasi-isothermal. The maximum wall-temperature difference $\Delta T = T_{max} - T_{min}$ is reported in Tab. 1 for each month: it is minimal in February/August (0.124 K) and maximal in May/November (0.492 K).

We can gain more insight by considering in Fig. 2b the time evolution of the temperature averaged on the four edges highlighted in Fig. 2a. The average temperature of the upper left edge, which is the closest to the ground surface, evolves with larger amplitude and different phase shift compared to that of the other edges, whose temperatures differ little from each other. More specifically, the phase shifts of the left upper edge (depth $d = 7.3\,\mathrm{m}$) and of the right upper edge (depth $d = 10.3\,\mathrm{m}$) are respectively 0.40 and 0.53 year. This is close to the values 0.41 and 0.58 year predicted by a 1D semi-infinite model for which the phase shift is $d\sqrt{\tau/(4\pi\alpha_r)}$. The complexity of the wall temperature fields thus results from the small 10° slope between the ground and the horizontal plane (see Fig. 1a). Consequences on the flow structure will be analysed in Sec. 4 by using these wall temperature fields as thermal boundary conditions in the LES.

3. Large-eddy simulation model

3.1. Governing equations

The air filling the cavity is assumed to be dry, transparent and at atmospheric pressure. Following the Boussinesq approximation, the physical properties of the fluid are assumed to remain constant, except in the buoyancy term of the momentum equation where the density is assumed to vary linearly with temperature. The natural convection flow induced in the cavity is therefore governed by the following dimensionless equations:

$$\boldsymbol{\nabla}^{*}.\boldsymbol{u}^{*} = 0, \tag{4}$$

$$\frac{\partial \boldsymbol{u}^{*}}{\partial t^{*}} + \boldsymbol{u}^{*}.\boldsymbol{\nabla}^{*}\boldsymbol{u}^{*} = -\boldsymbol{\nabla}^{*}p^{*} + PrT^{*}\boldsymbol{x}^{*} + \frac{Pr}{Ra^{0.5}}\boldsymbol{\nabla}^{*2}\boldsymbol{u}^{*} \tag{5}$$

$$\frac{\partial T^{*}}{\partial t^{*}} + \boldsymbol{u}^{*}.\boldsymbol{\nabla}^{*}T^{*} = \frac{1}{Ra^{0.5}}\boldsymbol{\nabla}^{*2}T^{*}, \tag{6}$$

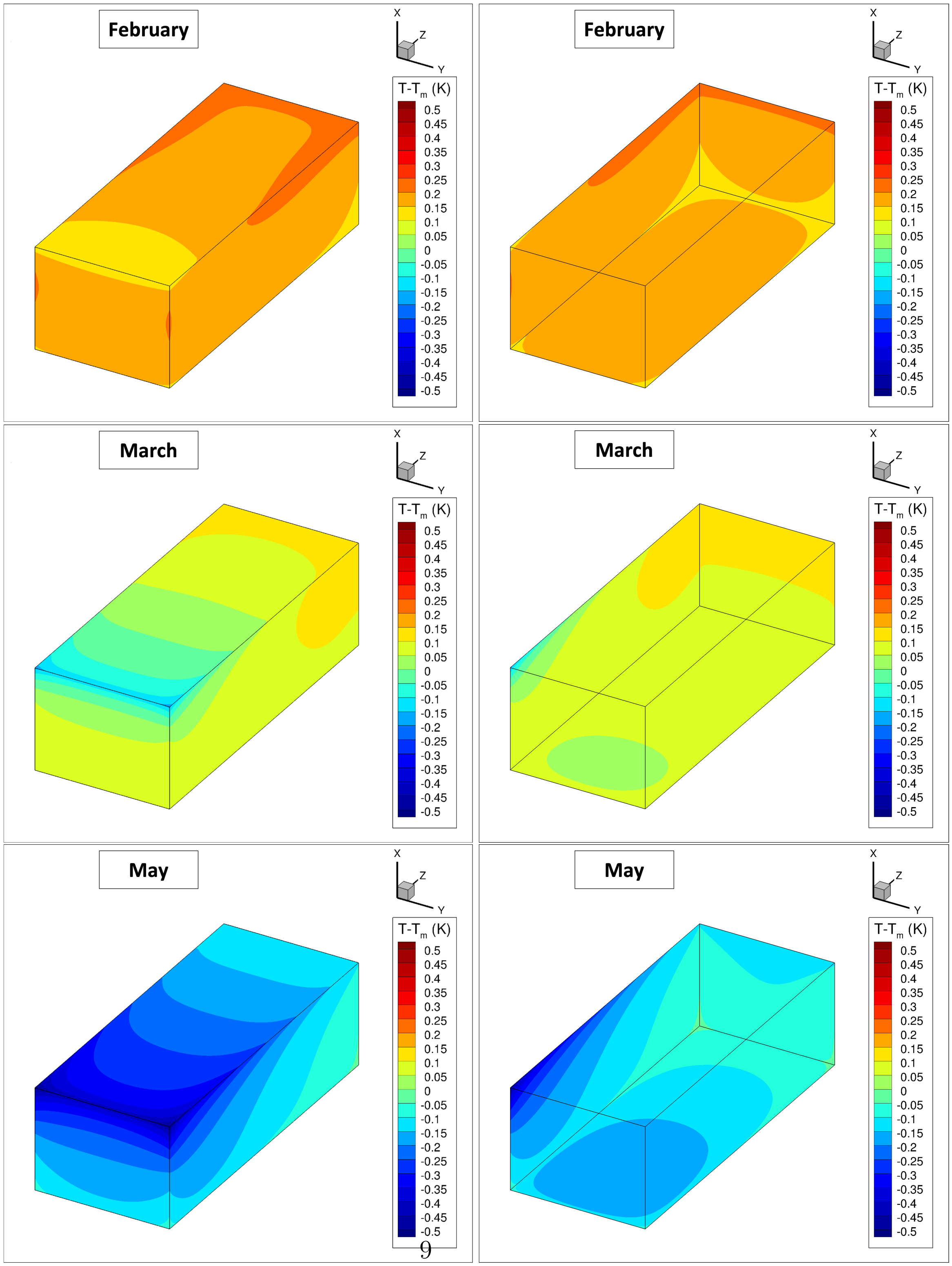

Figure 3: Wall temperature fields $T - T_m$ computed from the large–scale model for three months: February, March and May, from top to bottom. The left panels correspond to the upper ($X = L_X$), left ($Z = 0$) and front ($Y = L_Y$) cave walls. The right panels correspond to the bottom ($X = 0$), right ($Z = L_Z$) and back ($Y = 0$) cave walls.

where * denotes dimensionless variables and $\boldsymbol{u}$, p, T are respectively the velocity vector, the motion pressure and the temperature. Equations are made dimensionless using the reference height L_X, the reference time $t_{ref} = L_X^2/(\alpha Ra^{0.5})$, and the reference temperature scale ΔT. The reduced temperature thus reads $T^* = (T - T_0)/\Delta T$, where $T_0 = (T_{max} + T_{min})/2$ is the reference temperature. $Pr = \nu/\alpha = 0.712$, and $Ra = g\beta\Delta T L_X^3/(\alpha\nu)$ are respectively the Prandtl number, and the Rayleigh number, where $\alpha = 2.05 \times 10^{-5}\,\mathrm{m}^2.\mathrm{s}^{-1}$ is the thermal diffusivity, $\nu = 1.46 \times 10^{-5}\,\mathrm{m}^2.\mathrm{s}^{-1}$ is the kinematic viscosity and $\beta = T_0^{-1}$ is the thermal expansion coefficient.

Hydrodynamic and thermal boundary conditions at cave walls are zero velocity (no–slip) and one of the temperature fields provided by the large–scale model. Wall temperatures are assumed to be time–independent. This is justified by the large time scale associated with the time evolution of the wall temperature compared to the small characteristic time scale associated with the convection inside the cave. Indeed, the characteristic time scale of conduction in the rock for a depth equal to 7.3 m is about 2 years, which is of the same order as the period of 1 year characterizing the change of external boundary conditions, while the circulation time (or convection time), based on the computed velocities is of the order of a few minutes. The time required to reach statistically steady flows in the numerical simulations is of the order of 1 hour, which is also much smaller than one year.

One of the main outcome of the simulation is the distribution of the conductive flux at the walls, to be compared with the radiative flux from the large–scale model. The conductive flux through the walls in the gas phase reads

$$q_{con} = -\lambda \boldsymbol{\nabla} T \cdot \boldsymbol{n}, \tag{7}$$

where $\lambda = 2.51 \times 10^{-2}\,\mathrm{W.m}^{-1}.\mathrm{K}^{-1}$ is the air conductivity. The dimensionless counterpart of Eq. (7) is

$$Nu = -\boldsymbol{\nabla}^* T^* \cdot \boldsymbol{n}, \tag{8}$$

where $Nu = q_{con} L_X/(\lambda\Delta T)$ is the Nusselt number at the walls.

The values of ΔT, T_0 and Ra for the six cases considered in the LES are listed in Tab. 1. Notice that similar values of Ra may correspond to different wall temperature fields resulting in different flow structures, as will be seen in section 4.

Time	Month	ΔT (K)	T_0 (K)	Ra $\times 10^{-9}$
$0.11\,\tau$	August	0.124	284.985	2.13
$0.20\,\tau$	September	0.312	285.165	5.35
$0.37\,\tau$	November	0.492	285.419	8.41
$0.61\,\tau$	February	0.124	285.315	2.13
$0.70\,\tau$	March	0.312	285.135	5.35
$0.87\,\tau$	May	0.492	284.881	8.43

Table 1: Maximum temperature difference ΔT, reference temperature T_0 and Rayleigh number Ra for the six wall temperature fields used as boundary conditions in the LES ($\tau = 1\,$year).

3.2. Numerical methods

The large-eddy simulation (LES) approach is used in this study to save computational time. Simulations are performed using a Chebyshev pseudo-spectral method (detailed in Sec. 3.2.1), associated with a spectral vanishing viscosity (SVV) method (detailed in Sec. 3.2.2) to model the effects of the subgrid scales. In Sec. 3.3, we analyse the sensitivity of LES results to SVV parameters and we compare LES results with Direct Numerical Simulation (DNS) results in February, which corresponds to the smallest Rayleigh number investigated.

3.2.1. Chebyshev pseudo-spectral method

The flow governing equations are implemented in a spectral code close to the one developed by Xin and Le Quéré [23], using a Chebyshev collocation method for the three spatial dimensions. This type of spectral method reaches a high spatial accuracy at a reasonable numerical cost. It assumes that the required solution is represented on a finite basis of orthogonal functions. The basis functions considered for the spatial discretization are the Chebyshev polynomials, suitable for the development of non-periodic functions. A projection method is used to ensure the pressure-flow coupling: first, the momentum and heat equations are solved using the pressure field from the previous time step; second, a pressure correction term is calculated from a Poisson equation and the predicted velocity is corrected to force the velocity divergence free condition. Time integration is performed using a second-order semi-implicit temporal scheme, coupling a backward differentiation (BDF2) scheme for the linear diffusion terms and an Adams Bashforth extrapolation for the convective terms. Moreover, the computational domain is decomposed along the largest spatial direction (here the Z-horizontal direction) in order to perform parallel computations [24].

3.2.2. Spectral vanishing viscosity model

LES involves filtering the Navier-Stokes equations and solving only the large scales of a turbulent flow. The small scales of the flow are not solved but must be modeled. According to the filtering operation applied to the equations (4)-(6), additional non-linear terms are generated with supplementary unknowns to be modeled by expressing them in terms of the filtered variables. For the momentum and heat transfer equations, the dimensionless supplementary terms are the subgrid scale stress tensor $\boldsymbol{\nabla}^*.\boldsymbol{\tau}_{LES}{}^* = \boldsymbol{\nabla}^*.(\overline{\boldsymbol{u^*u^*}} - \overline{\boldsymbol{u^*}}\,\overline{\boldsymbol{u^*}})$ and the subgrid scale heat flux $\boldsymbol{\nabla}^*.\boldsymbol{q}_{LES}{}^* = \boldsymbol{\nabla}^*.(\overline{\boldsymbol{u^*}T^*} - \overline{\boldsymbol{u^*}}\,\overline{T^*})$ where $\overline{a}$ denotes the spatial filtering operator of the variable a. These terms are usually modelled as diffusion terms [25].

Conventional LES models based on a subgrid viscosity are not suited for spectral methods, and we rely in this work on the Spectral Vanishing Viscosity (SVV) method [26, 27], which has been specially developed for them. It consists in the introduction of an artificial dissipation term to ensure the spectral convergence, i.e. dissipate the high modes of the Chebyshev polynomial development. The main feature of the SVV method is to maintain the spectral accuracy, i.e. the exponential rate of convergence of the numerical solution [21]. This SVV method has been used for several applications such as turbulent channel flows [28], turbulent flows within rotating cavities [29] and turbulent wakes [30].

The SVV method is implemented in the form of a modified Laplacian operator combining the viscous and the SVV terms [21]. Hence, the modified Laplacian operator $\boldsymbol{\nabla}^2_{SVV}$ is given by

$$\boldsymbol{\nabla}^2_{SVV} = \boldsymbol{\nabla}.(1 + \nu^{-1}Q)\boldsymbol{\nabla}, \tag{9}$$

where Q is the viscosity kernel and ν is the actual viscosity (in dimensionless form, equal to $PrRa^{-0.5}$ for momentum and $Ra^{-0.5}$ for energy equation). The viscosity kernel acts on each spatial direction independently. In spectral space, it is given for the i^{th} direction by

$$\hat{Q}_i(k) = \epsilon_i e^{\frac{-(k-N_i)^2}{(k-M_i)^2}}, \qquad \text{if}\, k > M_i \tag{10}$$

$$\hat{Q}_i(k) = 0, \qquad \text{if}\, k \leqslant M_i \tag{11}$$

where k is the Chebyshev polynomial order, ϵ_i is the viscosity amplitude, N_i is the number of collocation points in the i^{th} direction and $M_i \leqslant N_i$ is the cut-off spectral mode. ϵ_i and M_i are the control parameters of the SVV method. The numerical modeling reduces by either increasing M_i or decreasing ϵ_i. It is worth noting that the same SVV parameters are used in the momentum equation and in the energy equation. This would be similar to considering a subgrid Prandtl number equal to one in a conventional LES model based on subgrid viscosity and diffusivity.

3.3. Numerical validation

In order to study the accuracy of the SVV approach, we carry out a sensitivity analysis on the SVV parameters M_i and ϵ_i and on the mesh size. To this aim, we focus on the simulation of February (see Tab. 1), which corresponds to the smallest Rayleigh number investigated here (the less turbulent case) and for which DNS is practicable with current computational resources.

In a first step, we set the mesh size to $N_X \times N_Y \times (N_Z \times N_p) = 160 \times 160 \times (20 \times 32)$ (LES$_{160}$ mesh), where $N_{X/Y/Z}$ is the number of collocation points in directions $X/Y/Z$ in each subdomain and N_p is the number of processors, and we vary M_i and ϵ_i as described in Tab. 2. The results are presented in terms of time-averaged variables over a dimensionless time period of 100. The time-averaged fluxes through each of the six walls of the cavity are computed at each time step. The flow field is assumed to be statistically steady when the sum of these six fluxes is less than 1% of the maximum one. In Tab. 2, we calculate for each set of SVV parameters the volume-averaged temperature ($\langle T^* \rangle$), the volume-averaged kinetic energy of the mean flow ($k^*_{kin} = \langle u^*_i \rangle \langle u^*_i \rangle / 2$), the volume-averaged turbulent kinetic energy ($k^*_{tur} = \left\langle u^{*'}_i u^{*'}_i \right\rangle / 2$), and the Nusselt number ($Nu = -\boldsymbol{\nabla} \langle T^* \rangle . \boldsymbol{n_{int}}$) averaged over the upper (X^*=1), left (Z^*=0), and side ((Y^*=0) walls separately ($\langle a \rangle$ and $a^{'}$ denote the time average and the fluctuation of a respectively). There is no influence of the SVV parameters on the average wall heat flux and the volume-averaged temperature in the system (the change is less than 1%). In addition, the SVV parameters have little effects on the kinetic energy of the mean flow (less than 3%) but significant effects (up to 10%) on the turbulent kinetic energy. Therefore, varying the SVV parameters has little influence on the time averaged fields as previously found in the application of turbulent wakes by Pasquetti [21].

In a second step, we fix the SVV parameters to $M_i = 3N_i/4$ and $\epsilon_i = 1/(4N_i)$ and consider two LES meshes: $160 \times 160 \times (20 \times 32)$ (LES$_{160}$) and

SVV parameters	$\langle T^* \rangle \times 10^2$	$k^*_{kin} \times 10^4$	$k^*_{tur} \times 10^4$	$Nu_{up,X^*=1}$	$Nu_{left,Z^*=0}$	$Nu_{sides,Y^*=0}$
$M = N/2$, $\epsilon = 1/2N$	5.370	2.865	2.368	-16.385	6.046	7.192
$M = 2N/3$, $\epsilon = 1/3N$	5.367	2.889	2.274	-16.351	6.049	7.196
$M = 3N/4$, $\epsilon = 1/4N$	5.350	2.803	2.547	-16.385	5.979	7.219
$M = 4N/5$, $\epsilon = 1/5N$	5.341	2.880	2.504	-16.431	5.978	7.219

Table 2: Sensitivity to the SVV parameters of the volume-averaged temperature, the volume-averaged kinetic energy of mean flow, the volume-averaged turbulent kinetic energy and the wall-averaged Nusselt number for February.

$240 \times 240 \times (20 \times 32)$ (LES$_{240}$). Results are compared with those of a DNS (no model or $M_i = N_i$ and $\epsilon_i = 0$) with a mesh of $320 \times 410 \times (32 \times 32)$ points. The time required to perform the simulation for the dimensionless time $\Delta t^* = 1000$ with the DNS approach using the available resources is approximately 128000 hours. With the LES approach using LES$_{160}$ and LES$_{240}$ meshes, the time decreases to 24576 hours and 55360 hours, respectively. In Tab. 3, the same averaged variables described in Tab. 2 are recalculated for each case. The results obtained with the LES$_{240}$ mesh are in good agreement with the DNS (differences below 10%), while results obtained with the LES$_{160}$ mesh show significant discrepancies with the DNS (up to 20%).

Case	$\langle T^* \rangle \times 10^2$	$k^*_{kin} \times 10^4$	$k^*_{tur} \times 10^4$	$Nu_{up,X^*=1}$	$Nu_{left,Z^*=0}$	$Nu_{sides,Y^*=0}$
DNS	5.760	2.540	2.710	-14.755	4.968	6.825
LES$_{240}$	5.610	2.638	2.998	-15.605	5.381	6.961
LES$_{160}$	5.350	2.803	2.547	-16.385	5.979	7.219

Table 3: Comparison between LES and DNS methods in terms of the volume-averaged temperature, the volume-averaged kinetic energy of mean flow, the volume-averaged turbulent kinetic energy and the average wall Nusselt number for February.

In order to get further insights on the accuracy of the SVV-LES model, we compare LES$_{240}$ results and DNS results for the local distribution of key quantities such as the Nusselt number and the turbulent kinetic energy. In Fig. 4,a and b, we present the evolution of the Nusselt number along a horizontal line at the upper wall ($X^* = 1$, $Y^* = 0.6604$) and along a vertical line at the left wall ($Y^* = 0.6604$, $Z^* = 0$), respectively. The LES$_{240}$ mesh provides satisfactory results compared to the DNS with a small overestimation at

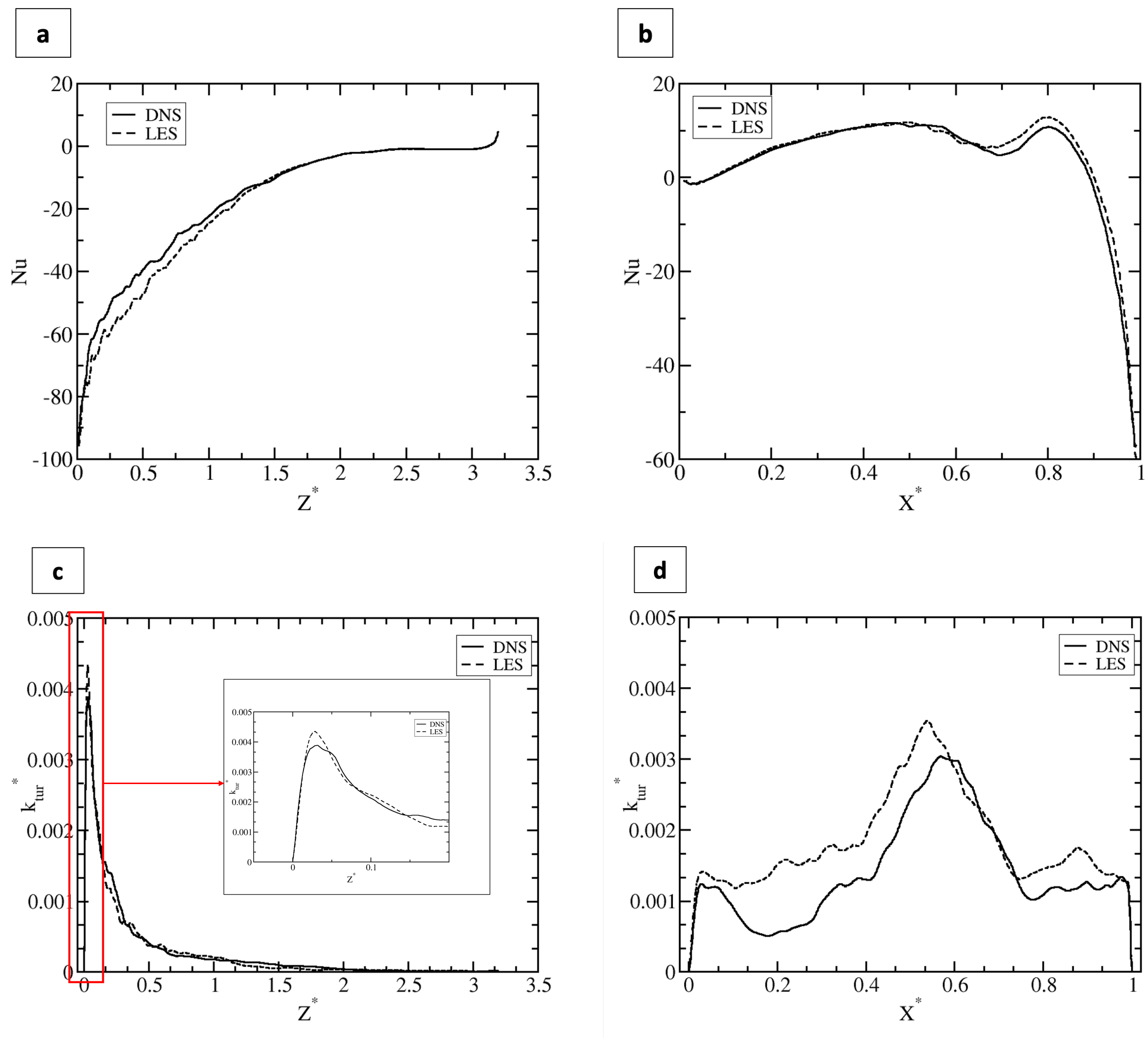

Figure 4: Nusselt number along the horizontal line $X^* = 1$, $Y^* = 0.6604$ (a) and the vertical line $Y^* = 0.6604$, $Z^* = 0$ (b) and turbulent kinetic energy along the horizontal line $X^* = 0.6$, $Y^* = 0.6604$ (c) and the vertical line $Y^* = 0.6604$ and $Z^* = 0.05$ (d) for February. The straight and dashed lines correspond to the DNS and LES_{240} results, respectively.

locations associated with significant turbulent fluctuations. In Fig. 4, c and d, we plotted the turbulent kinetic energy along a horizontal line ($X^* = 0.6$, $Y^* = 0.6604$) and along a vertical line ($Y^* = 0.6604$, $Z^* = 0.05$), where these turbulent fluctuations are significant. The agreement between LES_{240} and DNS is rather good within the vertical boundary layer (c) while discrepancies are more important near the bottom wall (d) with overpredictions of the tubulent kinetic energy up to a factor of 2. Consequently, the SVV method with the LES_{240} mesh preserves the heat flux at the walls but tends to overpredict the turbulent kinetic energy.

Since the main objective of this paper is to determine the role of turbulent convection on the heat fluxes at the cave walls and in order to save computational time, we use the LES_{240} mesh (CPU time savings of approximately 44% compared to DNS) and SVV parameters $M_i = 3N_i/4$ and $\epsilon_i = 1/(4N_i)$ for the simulation of all cases of Tab. 1.

4. Flow field analysis

4.1. One-cell and multiple-cell convection patterns

Figure 5 shows the streamlines of the mean airflow colored by the kinetic energy for each month studied, in the vertical Y mid-plane (the mean flow and mean temperature fields are mostly bidimensional thanks to the symmetry of the equations and boundary conditions with respect to the Y mid-plane). For all cases ascending or descending flows develop along the left and right vertical walls. They are connected through horizontal flows along the floor and the ceiling, giving rise to a primary rotating circulation in the cavity. However, we can define two distinct flow regimes depending on the period of the year: a one-cell regime in March, May and August (left panels in Fig. 5) characterized by a single large-scale circulation which extends over the entire cavity, and a multiple-cell regime in September, November and February (right panels in Fig. 5) for which the primary rotating flow near the walls is associated with more complex flow patterns within the core.

The different patterns can be schematically classified according to (i) the direction of rotation of the primary circulation along the walls, (ii) the number of cells in the bulk of the cavity. We are going to show that this classification results from the relative temperatures of the four edges mentioned in Sec. 2.1, as illustrated in Fig. 6 where rather cold edges are marked in blue and rather hot in red. Indeed, it can be seen in Fig. 2b, that for each month there is one edge that is significantly hotter or colder than the three

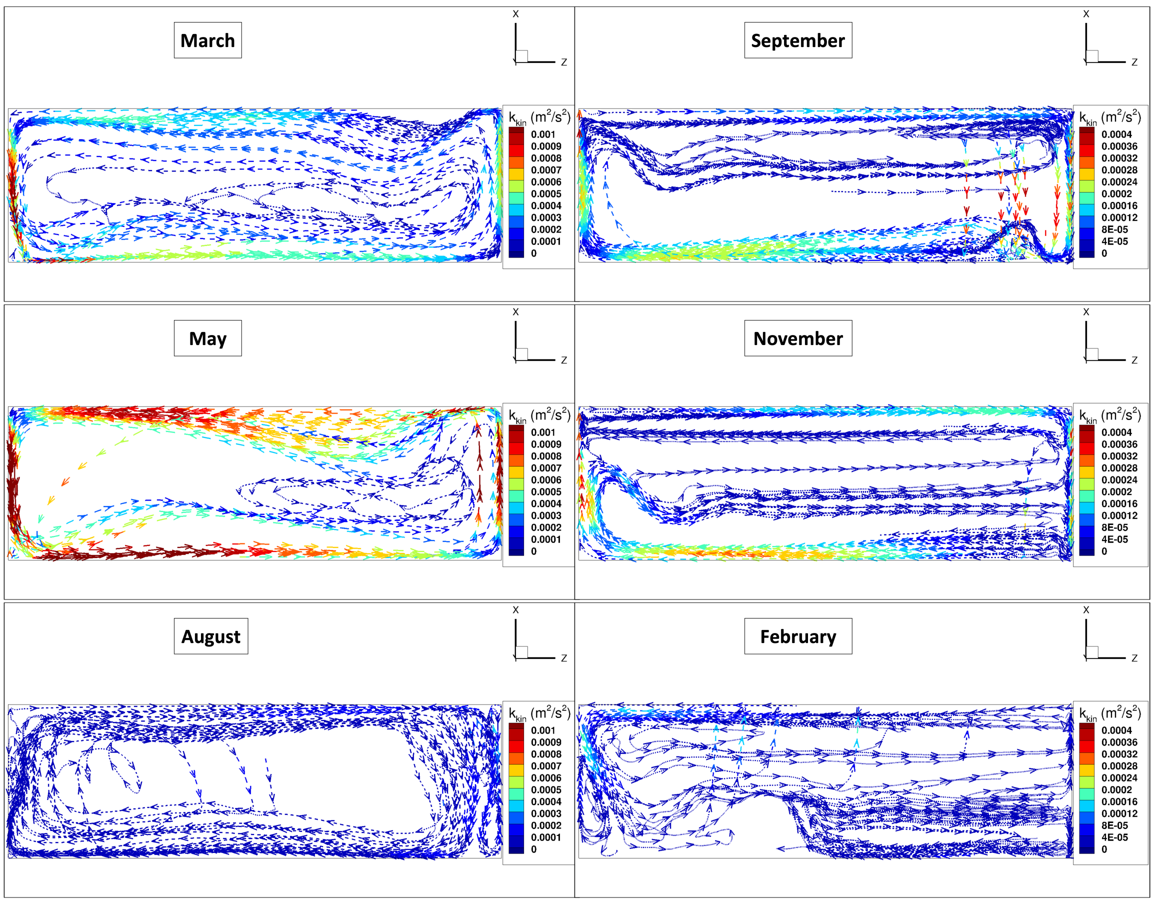

Figure 5: Flow streamlines colored by the kinetic energy of the mean flow. Streamlines are drawn from the Y mid-plane and then projected onto the Y mid-plane when they deviate from it.

others, which are almost at the same temperature. The direction of rotation of the primary circulation along the walls in the X-Z plane is determined by the sign of the horizontal temperature gradient along the Z axis. In March, May and February the right vertical wall is on average warmer than the left wall (the horizontal gradient is positive) giving rise to a counterclockwise rotation. Indeed, due to the buoyancy forces, the hot wall and the cold wall drive the air flow upward and downward, respectively. Conversely, the horizontal temperature gradient is negative in August, September and November resulting in a clockwise rotation. On the other hand, when the floor is on average warmer than the ceiling (March, May, August), the vertical temperature gradient is negative resulting in an unstable thermal stratification in the core and this corresponds to the one-cell regime. When the floor is on average colder than the ceiling (September, November, February), the vertical temperature gradient is positive resulting in a stable thermal stratification and this corresponds to the multiple-cell regime. For example in November, three convection cells of weak intensity are observed. The air layer adjacent to the left wall is heated then rises but the outer part of this layer is cooled by the core then slows down and generates a horizontal current at mid-height. This current travels through the core to the right side then splits with a part incoming to the downward flow adjacent to the cold wall and another part, slightly warmer, moving upward thus creating recirculation cells.

Based on this simplified analysis of thermal boundary conditions, we can conclude that the global circulation along the vertical and horizontal walls is governed by the temperature variations between the vertical walls, i.e., by the horizontal temperature gradient, whereas the nature of the regime, one-cell or multiple-cell, is determined by the temperature variations between the horizontal walls, i.e., by the vertical temperature gradient.

In the following, we analyse the flow dynamics, the thermal features and the turbulence level of the one-cell and mutliple-cell regimes. The volume-averaged kinetic energy of the mean flow, k_{kin}, the volume-averaged turbulent kinetic energy, k_{tur}, the maximum velocity, $\langle u \rangle_{max}$, and the volume-averaged standard deviation of the dimensionless mean temperature, $\sigma(\langle T^* \rangle)$, are given in Table 4 for each month. The one-cell regime is characterized by a strong mean flow compared to the multiple-cell regime, as indicated by relatively high k_{kin} and $\langle u \rangle_{max}$ values in May and March. In August, these quantities are comparable to those of September and November although the temperature difference ΔT is approximately 3 or 4 times smaller (see Tab. 1). The intense convection flow in the one-cell regime extends throughout the cavity

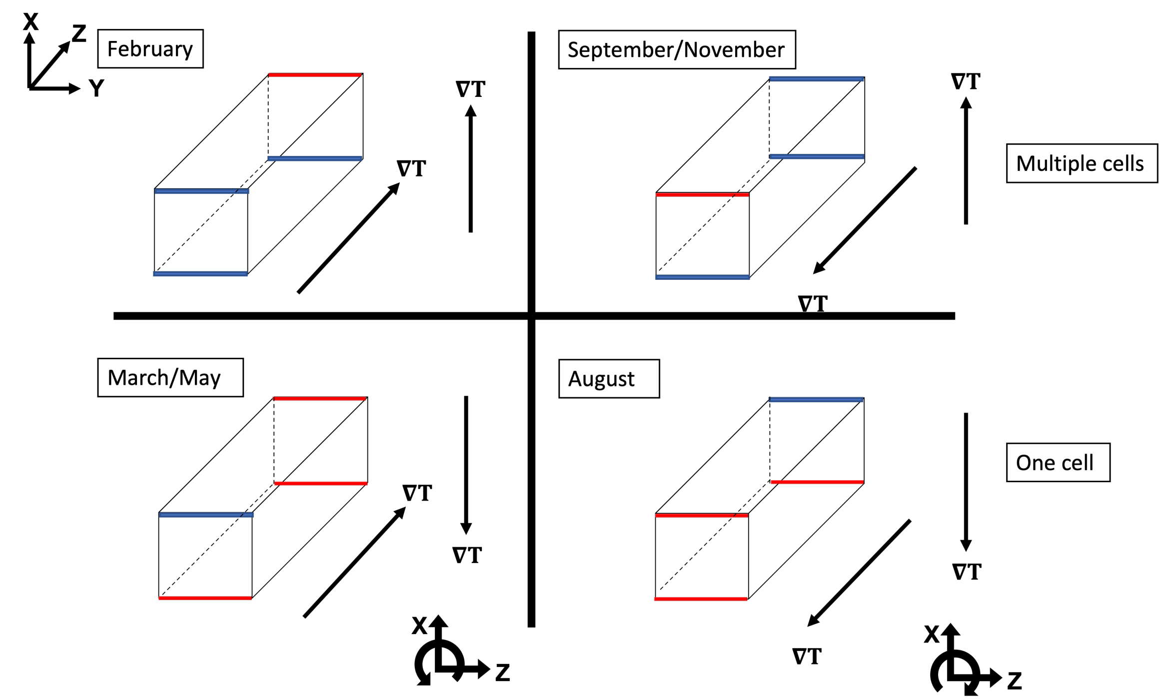

Figure 6: Simplified representation of thermal boundary conditions and associated flow regimes. Blue and red lines correspond to cold and hot edges, respectively.

Case	Regime	k_{kin} (m^2/s^2)	k_{tur} (m^2/s^2)	$\langle u \rangle_{max}$ (m/s)	$\sigma(\langle T^* \rangle)$
March	one-cell	1.6×10^{-4}	4.4×10^{-5}	0.076	0.018
May	one-cell	2.8×10^{-4}	9.3×10^{-5}	0.095	0.015
August	one-cell	3.5×10^{-5}	2.8×10^{-5}	0.045	0.011
September	multiple-cell	3.6×10^{-5}	8.8×10^{-6}	0.047	0.023
November	multiple-cell	3.1×10^{-5}	6.6×10^{-6}	0.050	0.044
February	multiple-cell	8.4×10^{-6}	1.0×10^{-5}	0.028	0.036

Table 4: Volume-averaged kinetic energy of the mean flow k_{kin}, volume-averaged turbulent kinetic energy k_{tur}, maximum velocity of the mean flow $\langle u \rangle_{max}$ and volume-averaged standard deviation of the dimensionless mean temperature $\sigma(\langle T^* \rangle)$ calculated for all months under study.

(see Fig. 5) leading to a strong mixing effect and thus the homogenisation of the temperature field. This gives rise to small values of $\sigma(\langle T^* \rangle)$ compared to the values related to the multiple-cell convection of weak intensity. To illustrate the analysis of the thermal feature, Fig. 7(top) displays the spatial distribution of the mean temperature in the Y mid-plane of the cavity. We focus on May (left panel) and November (right panel) as they correspond to the months with the greatest temperature amplitude (see Tab. 1) in the one-cell and multiple-cell regimes, respectively. In May, the temperature field is nearly isothermal thanks to the mixing effect of the large-scale convection cell. The temperature gradients are thus confined very close to the walls. By contrast, the temperature field in November shows significant temperature variations near the ceiling and a thermal stratification in the core related to the presence of the recirculation cells.

From the data reported in Table 4, we can see that the turbulent fluctuation level is higher in the one-cell regime than in the multiple-cell regime. It should be noted that, although the kinetic energy of the mean flow is very low in February, turbulent fluctuations are detected due to the presence of counter-rotating cells near the left wall (see Fig. 5). The spatial distribution of the turbulent kinetic energy is presented in Fig. 7 (bottom panels) for May and November. In May, significant turbulent fluctuations are noticeable in the lower left corner where the descending vertical boundary layer hits the floor and to a less extent in the upper right side. The asymmetry between the lower left and upper right corners is due to larger temperature gradients in the left part of the cavity than in the right part. In November, the turbulent kinetic energy is very small and turbulent fluctuations are detectable only in the left part of the cavity near the flow division and in the top right region where the downward flow in the cold boundary layer is sheared by the ascending recirculation flow (see Figure 5).

In order to visualize and compare the 3D turbulent structures in May and November, we make use of the Q-criterion $Q = [\Omega_{ij}\Omega_{ij} - S_{ij}S_{ij}]/2$ [31], where $\Omega_{ij} = [\partial u_i/\partial x_j - \partial u_j/\partial x_i]/2$ is the vorticity tensor and $S_{ij} = [\partial u_i/\partial x_j + \partial u_j/\partial x_i]/2$ is the strain tensor. This criterion compares the rates of rotation and deformation. Turbulent structures correspond to positive values of Q [32]. Figure 8 shows the Q-criterion colored by the kinetic energy of the mean flow for these two months, for a given instantaneous flow field in the asymptotic regime. Vortices almost spread everywhere in May, while they are restricted to regions near the left and right planes in November. It is interesting to note that the instantaneous flow is fully three-dimensional

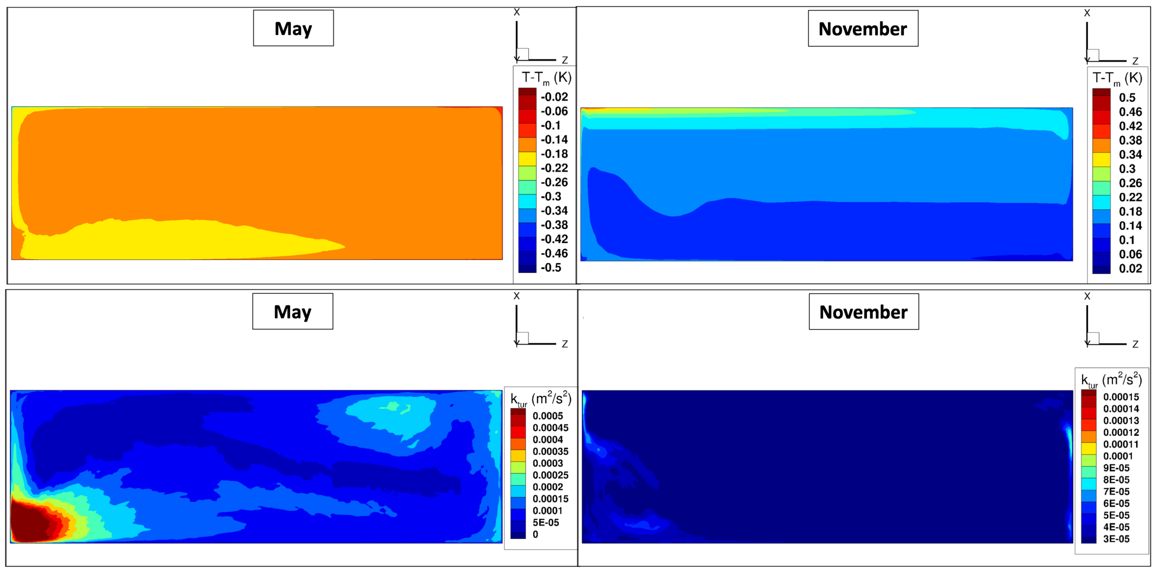

Figure 7: Mean temperature (top panels) and turbulent kinetic energy (bottom panels) fields in the Y mid-plane of the cavity for May and November.

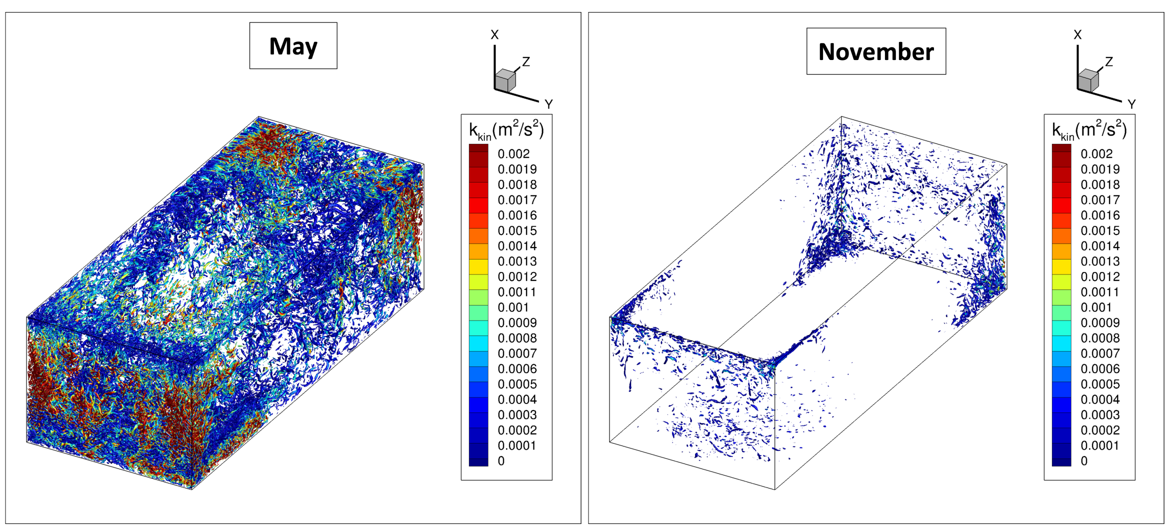

Figure 8: Isosurfaces of the Q-criterion colored by the kinetic energy of the mean flow for an instantaneous flow field for May and November. $Q = 1$ s^{-2} for all cases.

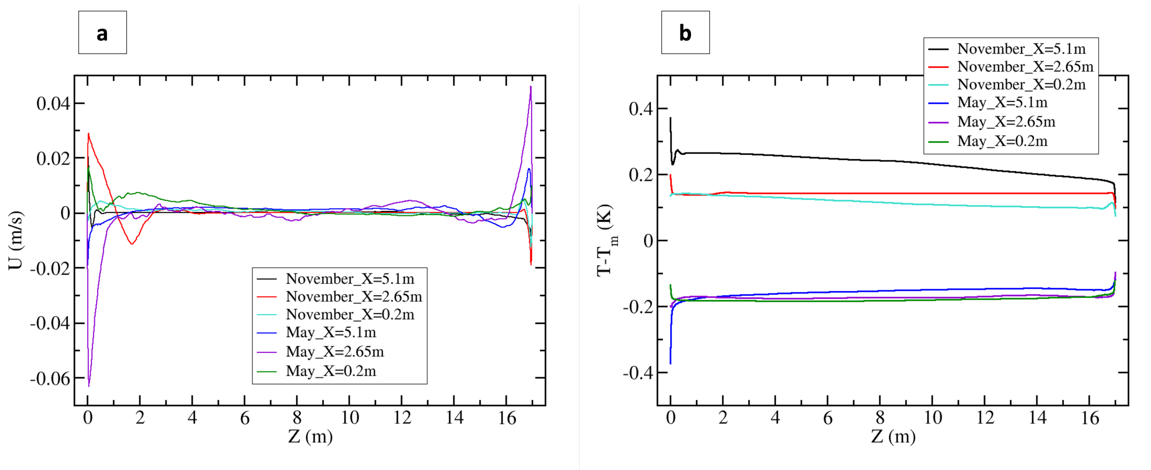

Figure 9: Horizontal profiles of the vertical velocity component U (a) and temperature (b) in the Y mid-plane for three different heights ($X = 0.2$ m $\approx 0.04L_X$, $X = 2.65$ m $= 0.5L_X$ and $X = 5.1$ m $\approx 0.96L_X$). The vertical walls are located at $Z = 0$ and $Z = 17$ m. May (one-cell regime) and November (multiple-cell regime) are presented.

for both months, though the main mean dynamics happen in the X-Z plane.

4.2. Near wall regions

To get a better insight into the flow structure in the near-wall region, we discuss in this section the temperature and velocity profiles along vertical or horizontal lines.

Fig. 9 presents horizontal profiles of the vertical velocity component U and the temperature in the Y mid-plane for three different heights ($X = 0.2$ m $\approx 0.04L_X$, $X = 2.65$ m $= 0.5L_X$ and $X = 5.1$ m $\approx 0.96L_X$), for May (one-cell regime) and November (multiple-cell regime). Velocity boundary layers are observed in Fig. 9 (a), ascending or descending according to the sign of the horizontal temperature gradients in the thermal boundary layers (see Fig. 9 (b)). It can be noted that in May, the horizontal temperature and velocity gradients change sign in the left bottom part ($X = 0.2$ m, $Z \approx 0$) due to the presence of a small vortex in the corner (see Figure 5). The thickness of the velocity and thermal boundary are estimated as follows. The thickness of the velocity boundary layer, δ_u, is referred as the distance from the wall to a point where the velocity reaches an extremum. The thickness of the thermal boundary layer, δ_θ, is referred as the distance from the wall where the temperature reaches 90 % of its value in the core. We find that

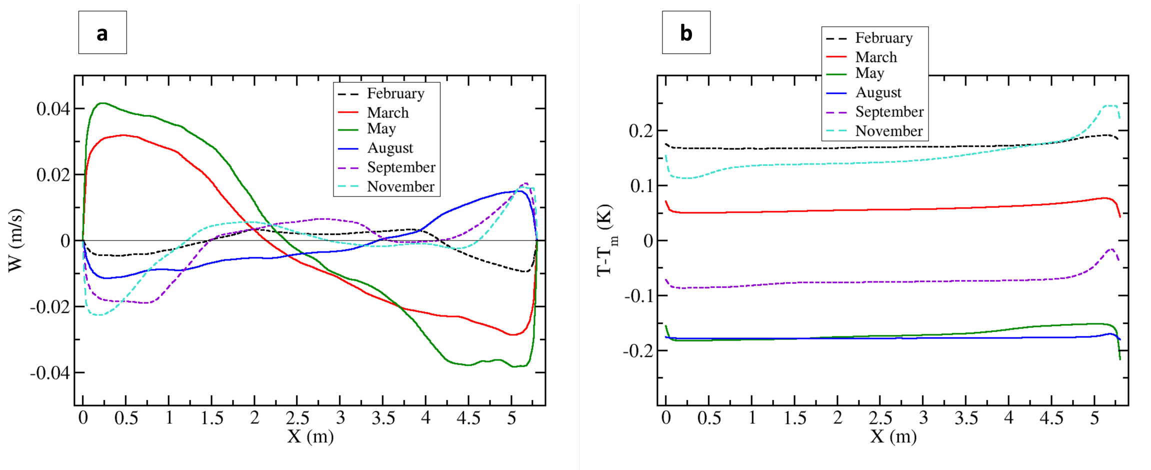

Figure 10: Vertical profiles of the horizontal velocity component W (a) and the temperature (b) along the vertical centerline ($Y = 0.5L_Y$, $Z = 0.5L_Z$) for the six months investigated. The horizontal walls are located at $X = 0$ and $X = 5.3$ m. The solid and dotted lines correspond to the one-cell and multiple-cell regime, respectively.

$\delta_u \sim \delta_\theta$ ranges from 4 cm to 8 cm, i.e., less than 0.5% of the cavity length ($L_Z = 17$ m).

As highlighted in subsection 4.1, Fig. 9 (b) shows that the core of the cavity is nearly isothermal in May whereas a stable vertical thermal stratification takes place in November, especially in the upper half of the cavity where a temperature difference of about 0.1 K is observed between the air at mid-height (red curve) and the air adjacent to the top wall (black curve).

Fig. 10 presents the horizontal velocity component W and the temperature profiles along the vertical centerline ($Y = 0.5L_Y$, $Z = 0.5L_Z$), in the one-cell regime for March, May and August (solid lines) and in the multiple-cell regime for February, September and November (dashed lines). In the one-cell regime, Fig. 10 (a) exhibits the large-scale circulation extending over the entire height of the cavity, with a reverse direction of rotation for August compared to March and May. By contrast, the core is almost motionless in the multiple-cell regime, with however small variations around zero that are the signature of the recirculations of low intensity. Temperature profiles (Fig. 10 (b)) confirm that the temperature gradients are confined in very thin layers (few centimeters thick, i.e., less than 1% of the cavity height ($L_X = 5.3$ m)) near the horizontal walls in the one-cell regime. In the multiple-cell regime, the temperature variations are observed near the ceiling for September and November, in a layer that extends over about 1 m with a maximum temperature located at a few tens of centimeters from the wall.

5. Heat transfer analysis

5.1. Wall conductive fluxes

In this subsection, we analyse the local heat transfer rates at the walls by quantifying the conductive wall heat flux q_{con} defined in Eq. (7). As the underlying physical mechanisms are very diverse, depending on the location on the wall or the month considered, we do not conduct this analysis in terms of dimensionless quantities; we aim to characterize the local heat transfer coefficient h in the Newton's law

$$q_{con} = h(T_{wall} - T_{gas}), \tag{12}$$

where T_{wall} is the local wall temperature and T_{gas} is the air temperature averaged over the entire domain.

In Fig. 11, q_{con} is plotted versus $T_{wall} - T_{gas}$ for the six months investigated and for each wall (each point corresponds to a given spatial location). Positive values correspond to heat transfer from the wall to the fluid. In the one-cell flow regime (left panels), we observe that the dependence of the conductive flux with $T_{wall} - T_{gas}$ is roughly linear. For a given month, a linear fit performed through the cloud of points (black line in the figures) allows to estimate empirically a single heat transfer coefficient h for all walls, ranging from $0.45\,\mathrm{W.m^{-2}.K^{-1}}$ (in August) to $0.76\,\mathrm{W.m^{-2}.K^{-1}}$ (in May), according to the magnitude of the convection flow. For the multiple cell regime (right panels), the conductive flux follows the same trend, except at the upper wall. The linear fit associated to all the walls except the upper one provides values of h ranging from 0.33 to $0.68\,\mathrm{W.m^{-2}.K^{-1}}$. At the upper wall, $q_{con} \neq 0$ when $T_{wall} - T_{gas} = 0$ which means that T_{gas} is not the relevant reference temperature for the surrounding air layer. The actual reference temperature T_{bulk} is such that $q_{cond} = 0$ for $T_{wall} = T_{bulk}$ in the Newton's law. It can be easily deduced from the graphs in Fig. 11 that the averaged gas temperature T_{gas} underestimates T_{bulk} by approximately 0.03 K in February, 0.1 K in September, and 0.15 K in November. This is in line with the analysis presented in the previous section. Indeed, we have shown that the air layer near the ceiling is warmer than the core region at T_{gas}, which implies that the reference temperature must be ajusted upwards.

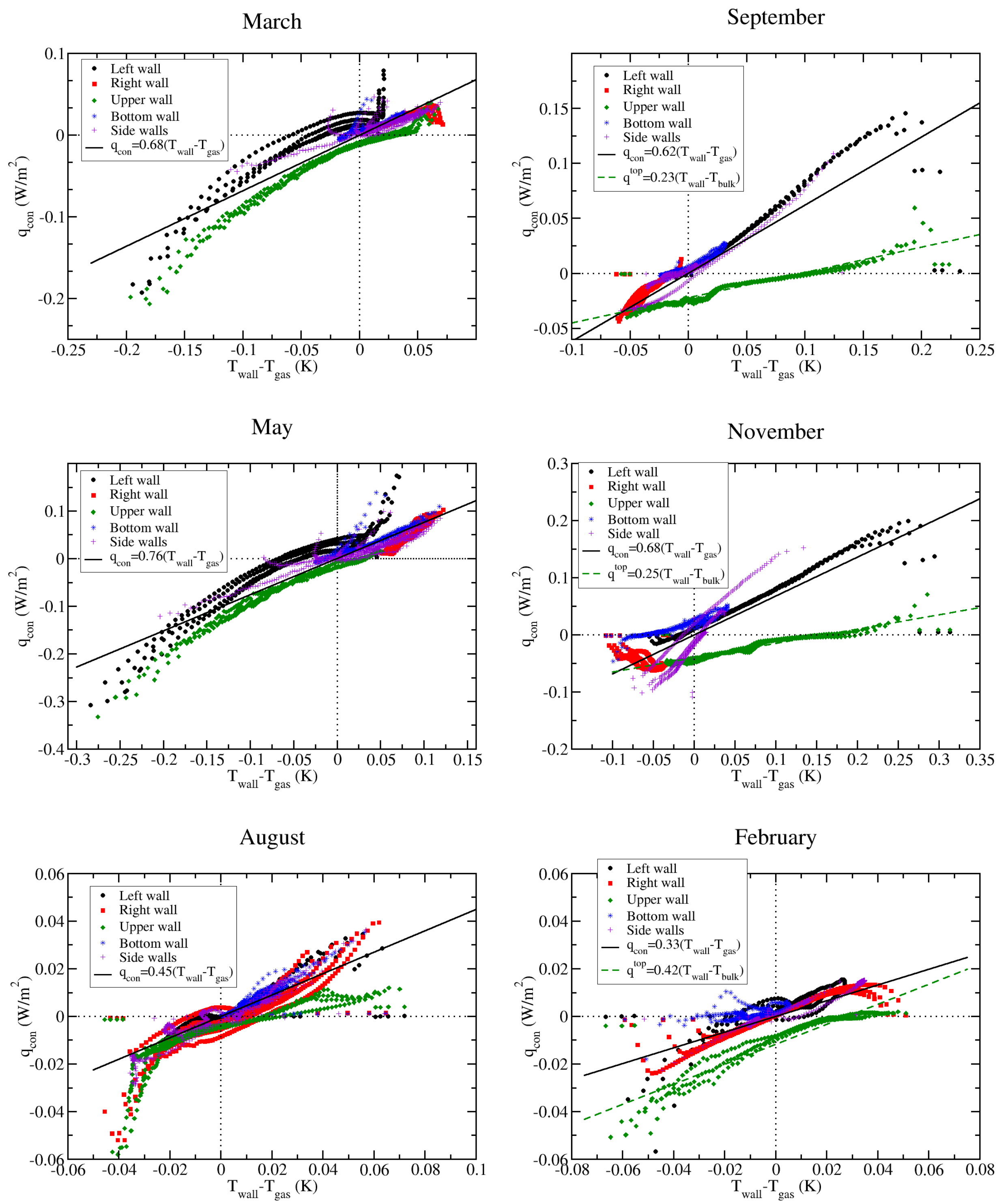

Figure 11: Cloud of points representing the local conductive heat flux at each wall versus the difference between the wall local temperature and the gas average temperature, for the six months investigated. Each point corresponds to a given spatial location on the wall. The black line represents the best linear fit of the cloud of points (with the exception of the top wall data in September, November and February). The green dashed line represents the best linear fit of the top wall in September, November and February, with T_{bulk} instead of T_{gas}.

By fitting both h^{top} and T_{bulk}, we get h^{top} ranging from $0.23\,\mathrm{W.m^{-2}.K^{-1}}$ (in September) to $0.42\,\mathrm{W.m^{-2}.K^{-1}}$ (in February). It is worthy to note that all the values of the heat transfer coefficient h remain in a limited range, from 0.23 to $0.76\,\mathrm{W.m^{-2}.K^{-1}}$. This is not surprising given that the Nusselt number usually scales as the Rayleigh number at the power 0.25 to 0.33 in natural convection [33], and thus increases slowly with the temperature differences between the cavity walls. Therefore, these estimations of the heat transfer coefficient might be used in a large-scale model coupling conduction in the rock, radiative transfer in the cavity, and natural convection described by the Newton's law (12). However, such approach raises the question of how to define the reference gas temperature in the Newton's law. In the case of complex non uniform temperature fields, relying on the averaged gas temperature may result in large errors on wall convective heat fluxes.

5.2. Wall total fluxes

The aim of this section is to show the distribution of the conductive flux q_{con} and to compare it to the distribution of the radiative flux q_{rad} and the total heat flux $q_{tot} = q_{con} + q_{rad}$. We focus here on the months with the highest conductive fluxes, i.e., May and November.

Fig. 12 presents the distribution of conductive (a and b), radiative (c and d), and total (e and f) fluxes at the walls for the month of May. The radiative flux largely dominates the conductive flux but the latter remains significant at several spots, especially in the left ceiling region, downstream the left vertical boundary layer and near the right bottom edge. The maximum total heat flux in the system reaches in absolute value 1.15 $\mathrm{W/m^2}$ and is concentrated around the left upper edge. The conductive flux represents 40% of this value.

We show in Fig. 13 the distribution of q_{con} (a and b), q_{rad} (c and d), and q_{tot} (e and f) for the month of November. It is worth noting that the radiative flux distribution in November is opposite to that in May (temperature distributions are opposite), while this is not the case for the conductive flux, sensitive to buoyancy. As in May, the system is mainly controlled by radiative fluxes but there is still significant conductive heat flux in the upper part of the left wall. Again, the maximum total heat flux reaches in absolute value 1.15 $\mathrm{W/m^2}$ and is concentrated at the left upper edge. The conductive flux represents about 35% of the total flux in the upper part of the left and side walls and in the majority of the right wall.

Heat transfer at the cavity walls is thus mainly dominated by the radiative heat flux, with the exception of some localized spots where both conductive

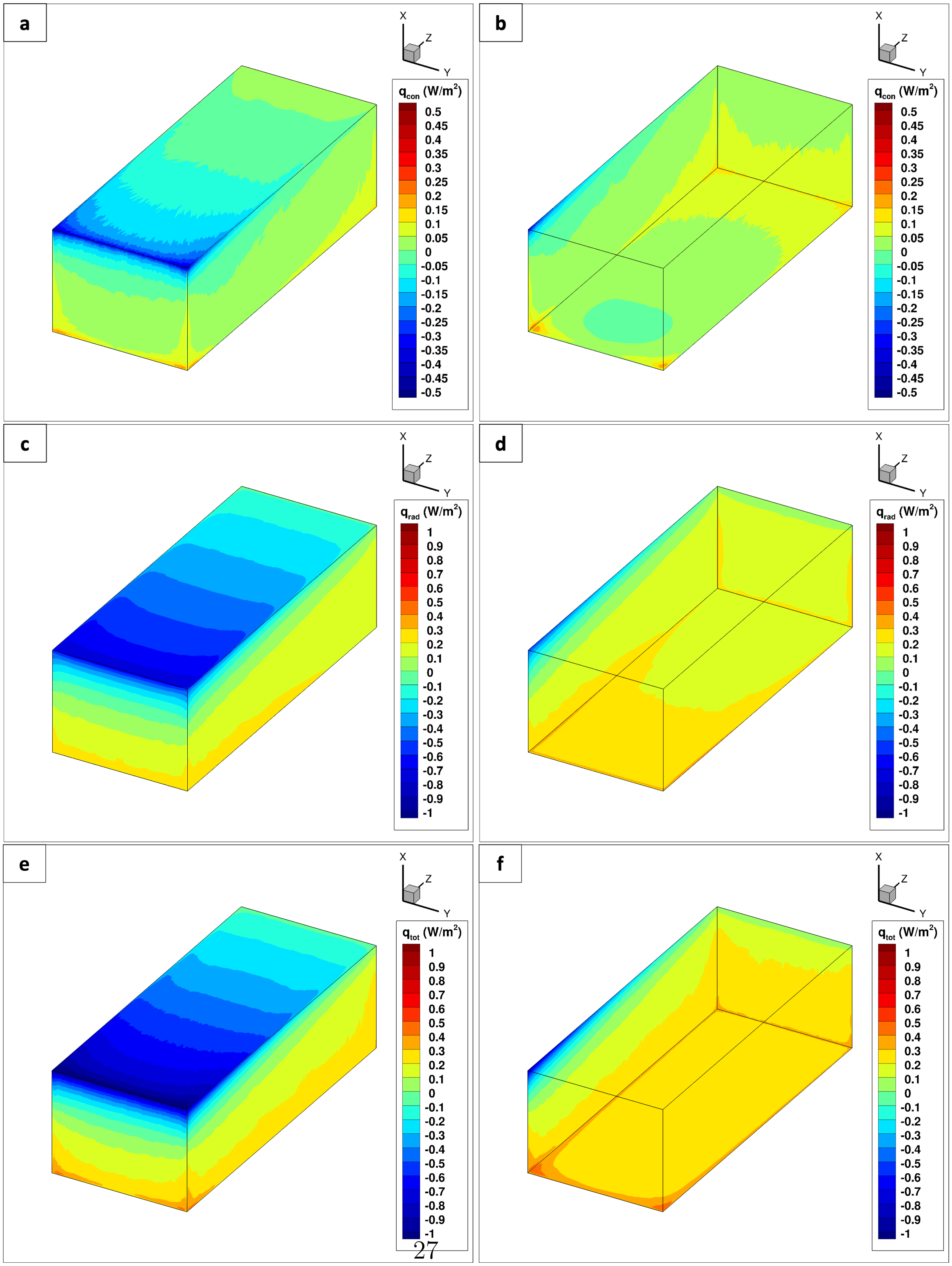

Figure 12: Spatial distribution of conductive (a and b), radiative (c and d) and total (e and f) heat fluxes at the walls for the month of May. The left part of the figure corresponds to the upper ($X = L_X$), left ($Z = 0$) and front ($Y = L_Y$) cave walls. The right part of the figure corresponds to the bottom ($X = 0$), right ($Z = L_Z$) and back ($Y = 0$) cave walls.

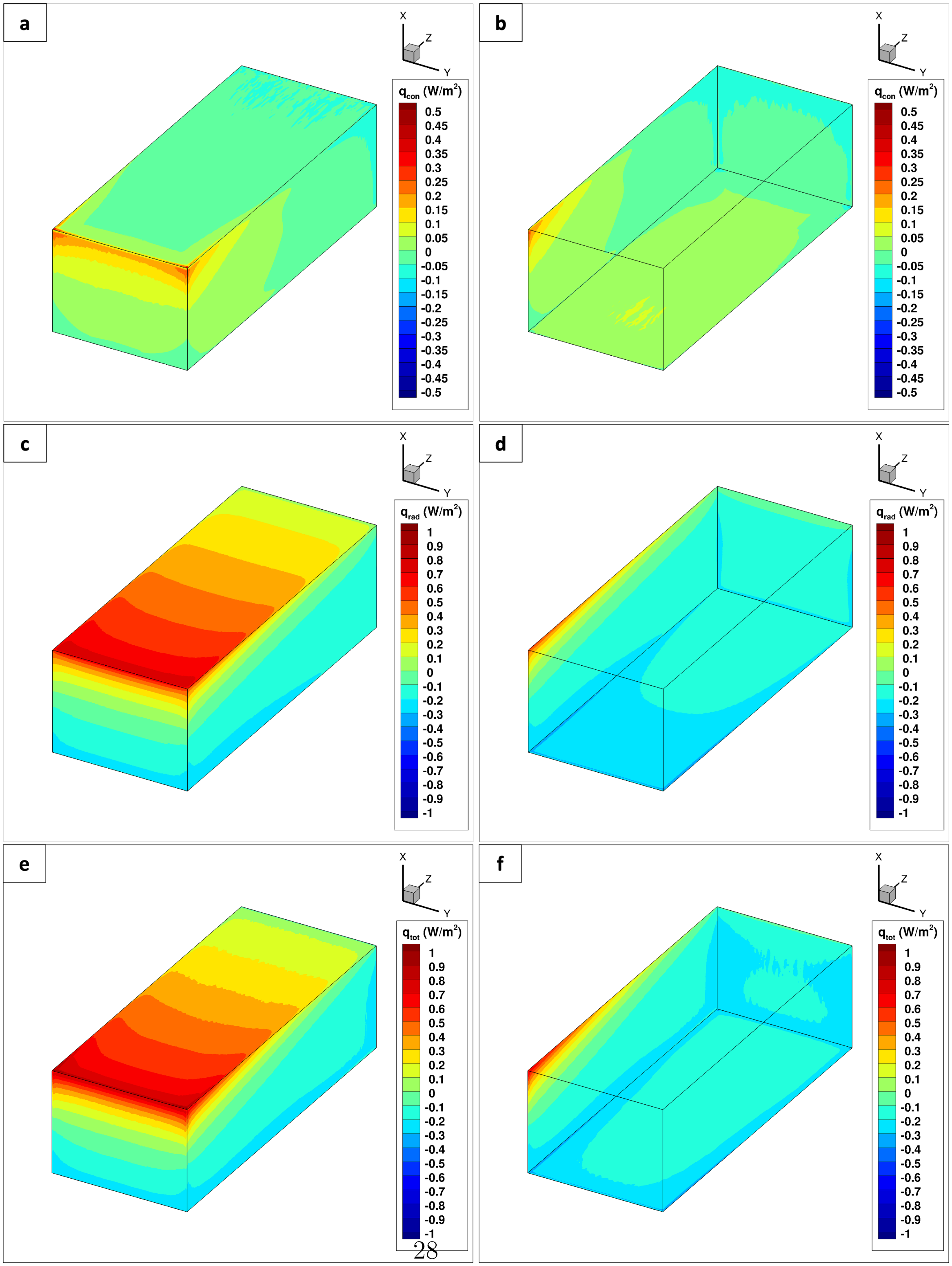

Figure 13: Spatial distribution of conductive (a and b), radiative (c and d) and total (e and f) heat fluxes at the walls for the month of November. The left part of the figure corresponds to the upper ($X = L_X$), left ($Z = 0$) and front ($Y = L_Y$) cave walls. The right part of the figure corresponds to the bottom ($X = 0$), right ($Z = L_Z$) and back ($Y = 0$) cave walls.

and radiative fluxes are on the same order. This conclusion must be tempered by the fact that dry air was considered. In humid caves, convection controls the heat flux associated with the latent heat of condensation and evaporation. This probably affects the total heat flux. Assuming that solutal buoyancy does not significantly modify the flow structure, the highest condensation flux should occur in May and the highest evaporation flux in November, in the region of the left upper edge in both cases. The effect of latent heat will be investigated in a future work.

6. Conclusion

In this paper, the effect of turbulent natural convection on heat transfer within a confined underground cavity was investigated using large eddy simulations based on the spectral vanishing viscosity method. Non-uniform wall temperatures computed from a large-scale model and representative of external climate condition at six times of the year were used as thermal boundary conditions.

We identified two different flow regimes: (i) a one-cell flow regime associated with strong convection and unstable mean vertical temperature gradient, (ii) a multiple-cell flow regime associated with weak convection and stable mean vertical temperature gradient. For each regime the mean direction of rotation of the flow is determined by the direction of the horizontal temperature gradient. The one cell flow regime (March, May, August) is characterized by a single-roll large-scale circulation, high turbulent fluctuation level and strong mixing resulting in the homogeneisation of the gas temperature. The multiple-cell flow regime (September, November, February) is characterized by two counter-rotating large-scale structures. It corresponds to a flow of weak intensity with low turbulent fluctuation level and a significant vertical temperature gradient in the air near the ceiling.

The values of the heat transfer coefficient in the Newton's law were calculated from the LES results. We found that the flow intensity and turbulence level have little influence on the heat transfer coefficient value. However, the definition of the reference gas temperature to be used in the Newton's law is a non trivial question in this problem with thermal boundary conditions defined from complex temperature fields. The choice of the average gas temperature is relevant when the air temperature is nearly uniform everywhere in the core of the cavity. Otherwise, significant errors in the prediction of wall heat fluxes may occur. This problem could likely be exacerbated by the complex geometry of natural caves, making even more necessary the use of CFD approaches as presented here.

Our method allows to determine if heat transfer at the cavity walls is dominated by conducto-convective or radiative fluxes. Moreover, places in the cavity and times of the year corresponding to intense heat transfer can be identified. In future works, we will consider the coupling with mass transport of water vapour in order to predict the conditions leading to intense condensation, a problem of great importance for the conservation of painted caves. In addition, given the significance of radiative fluxes, it might be worth investigating the effect of gas radiation associated with the presence of water vapour and carbon dioxide in the cave atmosphere.

Acknowledgements

This work was funded by the financial support of the LabeX LaSIPS (ANR-10-LABX-0032-LaSIPS) managed by the French National Research Agency under the "Investissements d'avenir" program (ANR-11-IDEX-0003-02). This work was granted access to the HPC resources of IDRIS under the allocation 2020-A0062B00209 attributed by GENCI (Grand Equipement National de Calcul Intensif). This work was also performed using HPC resources from the Mésocentre computing center of CentraleSupélec and École Normale Supérieure Paris-Saclay supported by CNRS and Région Île-de-France (http://mesocentre.centralesupelec.fr/).

References

[1] D. Ford, P. Williams, Karst hydrogeology and geomorphology, John Wiley & Sons, Ltd, 2007.

[2] I. J. Fairchild, A. Baker, Speleothem Science: From process to past environments, John Wiley & Sons, Ltd, 2012.

[3] Y. Lv, Y. Jiang, W. Hu, M. Cao, Y. Mao, A review of the effects of tunnel excavation on the hydrology, ecology, and environment in karst areas: Current status, challenges, and perspectives, Journal of hydrogeology 586 (2020) 124891.

[4] D. C. Culver, T. Pipan, The Biology of caves and other subterranean habitats, Oxford University Press, 2009.

[5] L. Quindos, A. Bonet, N. Diaz-Caneja, P. Fernandez, I. Gutierrez, J. Solana, J. Soto, E. Villar, Study of the environmental variables affecting the natural preservation of the Altamira Cave paintings located at Santillana del Mar, Spain, Atmospheric Environment 21 (1987) 551–560.

[6] P. Malaurent, J. Brunet, D. Lacanette, J.-P. Caltagirone, Contribution of numerical modelling of environmental parameters to the conservation of prehistoric cave paintings: the example of Lascaux Cave, Conservation and Management of Archaeological Sites 8 (2006) 59–76.

[7] M. Luetscher, P.-Y. Jeannin, Temperature distribution in karst systems: the role of air and water fluxes, Terra Nova 16 (2004) 344–350.

[8] M. Luetscher, B. Lismonde, P.-Y. Jeannin, Heat exchanges in the heterothermic zone of a karst system: Monlesi cave, Swiss Jura Mountains, J. Geophys. Res. 113 (2008) F02025.

[9] J. Brunet, J. Vouvé, P. Malaurent, Re-establishing an underground climate appropriate for the conservation of the prehistoric paintings and engravings at Lascaux, Conservation and Management of Archaeological Sites 4 (2000) 33–45.

[10] F. Bourges, P. Genthon, D. Genty, M. Lorblanchet, E. Mauduit, D. D'Hulst, Conservation of prehistoric caves and stability of their inner climate: Lessons from Chauvet and other French caves, Science of the Total Environment 58 (2019) 675–685.

[11] Y. Li, D. Ogura, S. Hokoi, J. Wang, T. Ishizaki, Behavior of an underground stone chamber with 3-d modeling to restrain water-related damage to mural paintings, Journal of Asian Architecture and Building Engineering 13 (2014) 499–506.

[12] S. Sánchez-Moral, V. Soler, J. Cañaveras, E. Sanz-Rubio, R. Van Grieken, K. Gysels, Inorganic deterioration affecting the Altamira Cave, N Spain: quantitative approach to wall-corrosion (solutional etching) processes induced by visitors, Science of The Total Environment 243-244 (1999) 67–84.

[13] E. Villar, P. Fernandez, L. Quindos, J. Solana, J. Soto, Temperature of rock surfaces in Altamira Cave (Spain), Cave Science 10 (1983) –.

[14] B. Guerrier, F. Doumenc, A. Roux, S. Mergui, P.-Y. Jeannin, Climatology in shallow caves with negligible ventilation: heat and mass transfer, International Journal of Thermal Sciences 146 (2019) 106066.

[15] N. Houillon, La dynamique du carbone inorganique dans le continuum sol-épikarstique-cavité du site de la grotte de Lascaux (France), Ph.D. thesis, University of Bordeaux (2016).

[16] J. Pallares, Laminar and turbulent Rayleigh-Bénard convection in a perfectly conducting cubical cavity, International Journal of Heat and Fluid Flow 23 (2002) 346–358.

[17] L. Soucasse, Ph. Rivière, A. Soufiani, S. Xin, P. Le Quéré, Transitional regimes of natural convection in a differentially heated cavity under the effects of wall and molecular gas radiation, Physics of Fluids 26 (2014) 024105.

[18] J. Brunet, P. Malaurent, R. Lastennet, Évolution de l'état hydrique d'une paroi de la Salle des Taureaux de la grotte de Lascaux : conséquences pour la conservation, Studies in conservation 51 (2006) 241–251.

[19] W. Rohsenow, J. Hartnett, Y. Cho, Handbook of heat transfer, McGraw-Hill (1998).

[20] D. Lacanette, S. Vincent, A. Sarthou, P. Malaurent, J.-P. Caltagirone, An Eulerian/Lagrangian method for the numerical simulation of incompressible convection flows interacting with complex obstacles: Application to the natural convection in the Lascaux Cave, International Journal of Heat and Mass Transfer 52 (2009) 2528–2542.

[21] R. Pasquetti, Spectral vanishing viscosity method for LES: sensitivity to the svv control parameters, Journal of Turbulence 6 (2005) 12.

[22] R. Siegel, J. Howell, Thermal Radiation Heat Transfer, Taylor & Francis, 2002.

[23] S. Xin, P. Le Quéré, An extended Chebyshev pseudo-spectral benchmark for the 8:1 differentially heated cavity, Numerical Methods in Fluids 40 (2002) 981–998.

[24] S. Xin, J. Chergui, P. Le Quéré, 3D spectral parallel multi-domain computing for natural convection flows, in: Springer (Ed.), Parallel Computational Fluid Dynamics, Lecture Notes in Computational Science and Engineering book series, Vol. 74, 2008, pp. 163–171.

[25] P. Sagaut, Large eddy simulation for incompressible flows, Springer-Verlag (2006).

[26] E. Tadmor, Convergence of spectral methods for nonlinear conservation laws, SIAM J. Numer. Anal. 26 (1) (1989) 30–44.

[27] Y. Maday, S. Kaber, E. Tadmor, Legendre pseudo-spectral viscosity method for nonlinear conservation laws, SIAM J. Numer. Anal. 30(2) (1993) 321–342.

[28] G. S. Karamanos, G. E. Karniadakis, A spectral vanishing viscosity method for large-eddy simulations, Journal of Computational Physics 163 (2000) 22–50.

[29] E. Severac, E. Serre, A spectral vanishing viscosity for the LES of turbulent flows within rotating cavities, Journal of Computational Physics 226 (2007) 1234–1255.

[30] R. Pasquetti, Spectral vanishing viscosity method for large-eddy simulation of turbulent flows, Journal of Scientific Computing 27 (2006) 365–375.

[31] F. Wu-Shung, L. Yu-Chih, L. Chung-Gang, Estimation of turbulent natural convection in horizontal parallel plates by the Q criterion, Int. Com. Heat Mass Trans. 45 (2013) 41–46.

[32] J. C. R. Hunt, A. A. Wray, P. Moin, Eddies, streams and convergence zones in turbulent flows, In Center for Turbulence Research, Proceedings of the Summer Program (1988).

[33] S. Grossmann, D. Lohse, Scaling in thermal convection: a unifying theory, Journal of Fluid Mechanics 407 (2000) 27–56.